ACS OMEGA

Open Access

http://pubs.acs.org/journal/acsodf

Article

Biological Renewable Cellulose-Templated $Zn_{1-X}Cu_XO/Ag_2O$ Nanocomposite Photocatalysts for the Degradation of Methylene Blue

Biruktait Ayele Lemecho, Dinsefa Mensur Andoshe, Noto Susanto Gultom, Hairus Abdullah, Dong-Hau Kuo, Xiaoyun Chen, Temesgen D. Desissa, Demeke Tesfaye Wondimageng, Yi-nan Wu, and Osman Ahmed Zelekew*

Cite This: *ACS Omega* 2024, 9, 13714−13727

Read Online

ACCESS | Metrics & More | Article Recommendations

ABSTRACT: Herein, Cellulose-templated $Zn_{1-X}Cu_XO/Ag_2O$ nanocomposites were prepared using biological renewable cellulose extracted from water hyacinth (*Eichhornia crassipes*). Cellulose-templated Cu-doped ZnO catalysts with different amounts of Cu as the dopants (1, 2, 3, and 4%) were prepared and denoted CZ-1, CZ-2, CZ-3, and CZ-4, respectively, for simplicity. The prepared catalysts were tested for the degradation of methylene blue (MB), and 2% Cu-doped ZnO (CZ-2) showed the best catalytic performance (82%), while the pure ZnO, CZ-1, CZ-3, and CZ-4 catalysts exhibited MB dye degradation efficiencies of 54, 63, 65, and 60%, respectively. The best catalyst (CZ-2) was chosen to further improve the degradation efficiency. Different amounts of $AgNO_3$ (10, 15, 30, and 45 mg) were used for the deposition of Ag_2O on the surface of CZ-2 and denoted CZA-10, CZA-15, CZA-30, and CZA-45, respectively. Among the composite catalysts, CZA-15 showed remarkable degradation efficiency and degraded 94% of MB, while the CZA-10, CZA-30, and CZA-45 catalysts showed 90, 81, and 79% degradation efficiencies, respectively, under visible light within 100 min of irradiation. The enhanced catalytic performance could be due to the smaller particle size, the higher electron and hole separation and charge transfer efficiencies, and the lower agglomeration in the composite catalyst system. The results also demonstrated that the Cu-doped ZnO prepared with cellulose as a template, followed by the optimum amount of Ag_2O deposition, could have promising applications in the degradation of organic pollutants.

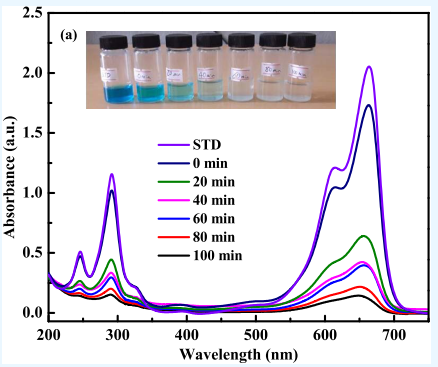

1. INTRODUCTION

Recently, the effluents of persistent organic pollutants in the environment, due to industrialization have become major sources of water pollution.[1] Particularly, the discharge of toxic organic pollutants into the environment could have adverse effects on human health.[2,3] For these reasons, wastewater treatment strategies using appropriate methods, such as adsorption, chemical redox reaction, photocatalytic degradation, and electrooxidation, have been implemented.[4−7] Among them, advanced oxidation processes (AOPs) are promising methods in which a complete degradation of emerging contaminants into carbon dioxide and water can be achieved.[8,9] For this purpose, different strategies such as ozonation, Fenton-based reactions, and photocatalysis methods have been utilized.[10−13]

Recently, photocatalysis has attracted tremendous attention in environmental remediation technology.[14,15] Different types of photocatalysts have been utilized for wastewater treatment using photocatalysis systems.[16−19] Among them, ZnO is the most studied semiconductor due to its high stability, low cost, and nontoxicity.[20] However, the wider band gap and higher recombination rates of the photogenerated charge carriers hinder its photocatalytic activity under visible light.[21] Hence, the modification of ZnO with different techniques such as doping or heterojunction formation to inhibit the photogenerated charge carrier recombination rates and expand the visible light absorption ranges have been reported.[22−24] According to previous reports, doping with copper is the best technique to improve photocatalytic efficiencies because of its unique interaction properties with ZnO.[25] In addition to doping, heterojunction formation with different semiconductors has been also reported.[26−28] Among them, the p-type Ag_2O semiconductor is a promising candidate due to its narrow band gap energy and facile preparation method.[29] However, Cu doping into ZnO or the formation of only Ag_2O/

Received: October 14, 2023
Revised: January 25, 2024
Accepted: February 29, 2024
Published: March 13, 2024

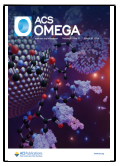

ZnO may not be sufficient to improve the catalytic performance of ZnO. Hence, metal doping together with heterojunction formation in the ZnO semiconductor catalyst system could help improve the catalytic efficiency. Not only doping or heterojunction formation, but also the utilization of biological renewable resources as templates have been reported to improve the catalytic performance of the photocatalyst.[30] As reported, the utilization of biological renewable resources in the preparation of the catalysts prevents agglomeration and decreases the particle size.[31,32]

Recently, ZnO has been prepared using biological renewable resources.[33−37] Among the biological renewable resources, cellulose is the best candidate due to its high hydroxyl functional groups in its structure. For example, Ag_2O/TiO_2-nanotubes with natural cellulose were fabricated.[38] Similarly, Cu-doped ZnO was also prepared by using Whatman filter paper as a template through the combustion method.[39] However, it is recommended that the sources of cellulose be cheap and unwanted plants, such as water hyacinth. As reported, water hyacinth is a very recent spreading weed in a water environment and has become a dangerous plant for the survival of water bodies. However, it is important to convert this unwanted plant into more useful products and applications.[40,41] Based on the above considerations, we aimed to design a cellulose-templated metal-doped ZnO/Ag_2O nanocomposite for the degradation of organic pollutants.

Herein, we prepared a $Zn_{1-X}Cu_XO/Ag_2O$ nanocomposite using natural cellulose extracted from hyacinth water as the template. The prepared catalysts were characterized and tested for MB degradation under visible light irradiation. Moreover, the effect of calcination temperature on the degradation efficiency was also studied. It is expected that the $Zn_{1-X}Cu_XO/Ag_2O$ nanocomposite prepared with optimum amounts of Cu as a dopant, followed by Ag_2O deposition, would have a higher catalytic efficiency. The enhanced catalytic efficiency could be due to the smaller particle size, the higher electron and hole separation and charge transfer efficiencies, and the lower agglomeration in the composite catalyst system.

2. MATERIALS AND METHODS

2.1. Chemicals and Reagents. Zinc nitrate hexahydrate ($Zn(NO_3)_2{\cdot}6H_2O$; Sigma-Aldrich, 98%), copper nitrate trihydrate ($Cu(NO_3)_2{\cdot}3H_2O$; Loba Chemie, 95%), silver nitrate ($AgNO_3$; Loba Chemie, 99%), sodium hydroxide (NaOH; Sigma-Aldrich, 98%), Methylene Blue ($C_{16}H_{18}ClN_3S$; Loba Chemie, 95%), ethanol (CH_3CH_2OH; 99%), and sodium chlorite ($NaClO_2$; Loba Chemie, 98%) were obtained. All chemicals and reagents were used without further purification.

2.2. Extraction of Cellulose. Water hyacinth was collected from Lake Koka, Ethiopia. The collected sample was washed with distilled water, dried in an oven at 60 °C for three consecutive days, and crushed into a powder. The powder was used for the extraction of cellulose according to a literature report with modifications.[42] In the extraction process, 34 g of water hyacinth powder was dewaxed with a 2:1 (v/v) mixture of toluene/ethanol solution for 6 h. The dewaxed powder was bleached with 3% sodium chlorite solution under acidic conditions, maintained for 3 h at 80 °C, and then allowed to settle overnight. The process was repeated twice and washed with distilled water until a neutral pH was reached. Hemicellulose was removed by treatment with 1 wt % NaOH solution at 60 °C for 24 h. The sample was washed with distilled water. Lignin was also removed by further treatment with 1 wt % sodium chlorite solution under acidic conditions with stirring at 75 °C for 48 h. The sample was washed with distilled water. The remaining hemicellulose was also removed by treatment with a 5% NaOH solution at 55 °C for 24 h under continuous stirring. Finally, the mixture was centrifuged and washed with distilled water until it was free from alkali.

2.3. Preparation of Cellulose-Templated Cu-Doped ZnO. Cu-doped ZnO ($Zn_{1-x}Cu_xO$) catalysts (x = 0.01, 0.02, 0.03, and 0.04) were synthesized by a green coprecipitation method using cellulose as a template and denoted CZ-1, CZ-2, CZ-3, and CZ-4, respectively. In a particular procedure, 0.5 g of cellulose was mixed with 100 mL of distilled water under stirring for 10 min. Then, 7.20 g of Zn $(NO_3)_2{\cdot}6H_2O$ and 0.12 g of Cu $(NO_3)_2{\cdot}3H_2O$ were added to the mixture containing the cellulose template. The mixed solution was then stirred under a magnetic stirrer for 1 h to form an aqueous solution. Then, a 2 M NaOH solution was added dropwise until the pH of the solution reached 10. The obtained precipitate was centrifuged, washed with distilled water and ethanol, and dried in an oven at 80 °C for 24 h. Finally, the obtained powder was calcined at 600 °C for 2 h to obtain the desired CZ-2 ($Zn_{0.98}Cu_{0.02}O$) catalyst. The same procedure was used to obtain all CZ-1, CZ-3, and CZ-4 catalysts, except that the amounts of precursors were varied. Pure ZnO and $Zn_{0.98}Cu_{0.02}O$ without cellulose were synthesized via the same procedure for comparison purposes. Calcination at 500 and 700 °C was also performed for optimization purposes.

2.4. Synthesis of Cellulose-Templated $Zn_{1-X}Cu_XO/Ag_2O$ Nanocomposite Catalysts. $Zn_{0.98}Cu_{0.02}O/Ag_2O$ nanocomposite catalysts were synthesized by a simple coprecipitation method. In a particular procedure, 100 mg of $Zn_{0.98}Cu_{0.02}O$ powder was dispersed in 2.5 mL of distilled water and sonicated for 30 min. Then, 15 mg of $AgNO_3$ was dissolved in another 2.5 mL of distilled water, dropped into the $Zn_{0.98}Cu_{0.02}O$ dispersed solution, and continuously stirred for 30 min. Then, 10 mL of 0.06 M NaOH was dropped under continuous stirring for about 10 min. The resulting powder was collected via centrifugation, washed, and dried at 80 °C for 24 h. The resulting composite catalyst was denoted CZA-15. Similarly, different amounts of $AgNO_3$ (10, 30, and 45 mg) were loaded onto $Zn_{0.98}Cu_{0.02}O$ and denoted CZA-10, CZA-30, and CZA-45, respectively. Furthermore, pure Ag_2O was also synthesized using the same procedure for comparison.

2.5. Characterization. Fourier transform infrared spectroscopy (FTIR-6600 type A) was used to examine the bonding and functional groups of the samples in the range of 4000−400 cm^{-1}. An X-ray diffractometer (Shimadzu XRD-7000) with Cu Kα radiation (λ = 1.5406 Å), operating in the range of 2θ = 20−80°, was used to determine the crystallinity and phases of the samples. The morphologies of the samples were examined by field-emission scanning electron microscopy (FE-SEM, JSM 6500F, JEOL) and transmission electron microscopy (TEM) (FEG TEM Tecnai G2 F30). X-ray photoelectron spectroscopy (XPS) (ESCALAB 250) was used to examine the chemical states of the sample. A Shimadzu-3600 plus UV−vis spectrophotometer was used to analyze the concentration of the MB dye at a maximum wavelength of 664 nm. A Shimadzu-3600 plus UV−vis spectrophotometer was used to measure UV−vis diffuse reflectance spectra (DRS) by using $BaSO_4$ as a reference.

2.6. Electrochemical Measurements. Electrochemical impedance spectroscopy (EIS) measurements were performed using a potentiostat SP-300 logic instrument in the frequency

https://doi.org/10.1021/acsomega.3c08051
ACS Omega 2024, 9, 13714−13727

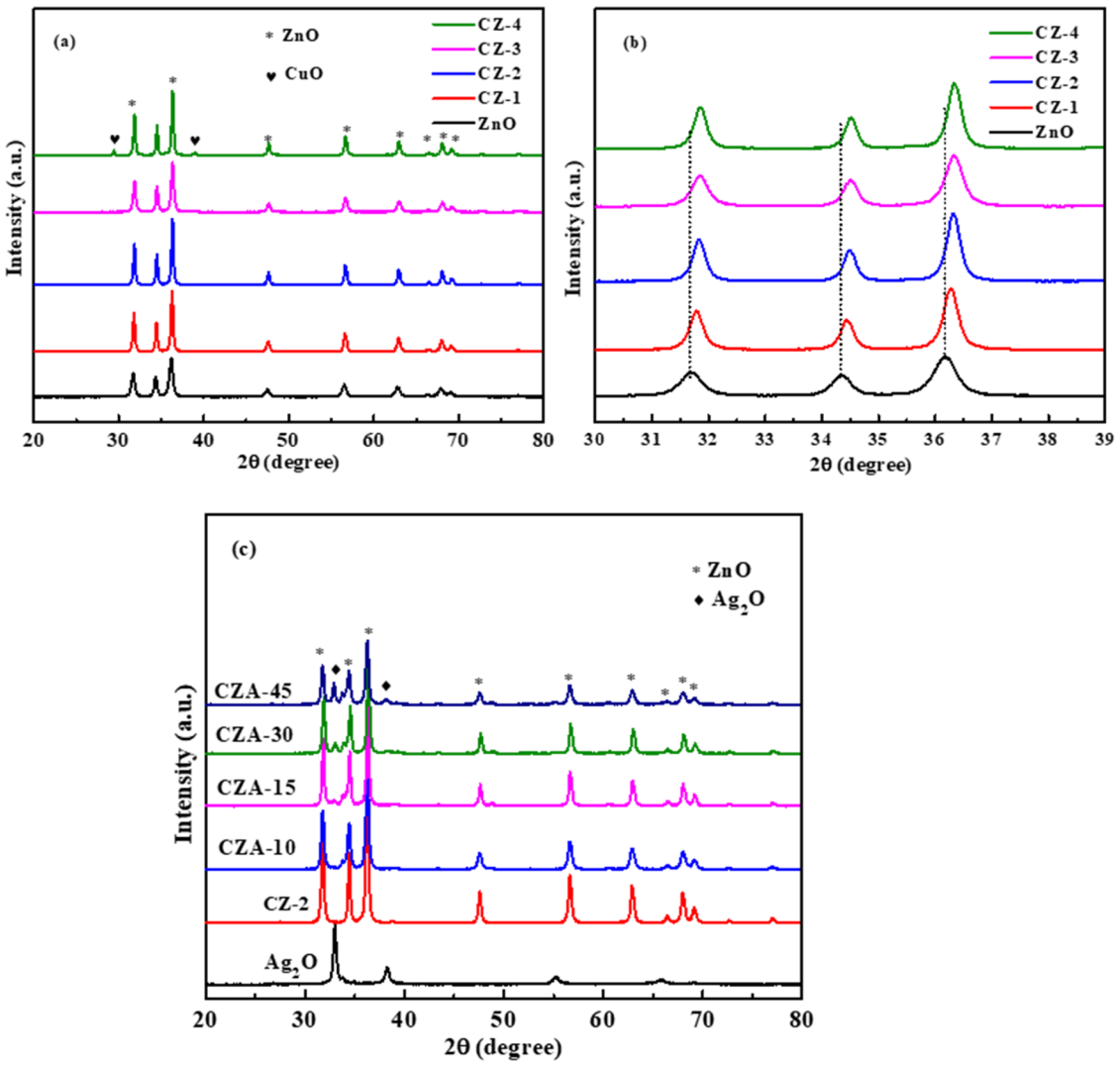

Figure 1. (a, b) XRD peaks and enlarged diffraction peaks of the pure ZnO and cellulose-templated $Zn_{1-X}Cu_XO$ samples. (c) XRD peaks of the pure Ag_2O and cellulose-templated $Zn_{1-X}Cu_XO/Ag_2O$ nanocomposites.

range of 10 mHz−100 kHz. Ag/AgCl and Pt were used as reference and counter electrodes, respectively. Then, 5 mg of the prepared catalyst was dispersed in the Nafion solution and ultrasonicated to prepare the working electrode. After that, 100 μL of the prepared ink was dropped onto a glassy carbon electrode and dried at room temperature. Mott−Schottky (M−S) measurements were also performed using a potentiostat SP-300 logic instrument at a frequency of 7 kHz.

2.7. Photocatalytic Activity Measurements. The photocatalytic experiments were conducted according to a literature report.[43] Typically, 25 mg of the catalyst was dispersed in 125 mL of MB dye (10 ppm). The solution was stirred for 30 min in the dark to reach adsorption/desorption equilibrium between the catalyst and pollutant. Then, the solution was irradiated under visible light illumination (150 W halogen lamp) with continuous stirring. In every 20 min time interval, aliquots were withdrawn and centrifuged. Finally, the concentration of MB dye was analyzed using a UV−vis spectrophotometer (UV−vis-3600 plus Shimadzu).

The reusability of the catalyst was determined as follows. In a particular procedure, 125 mg of CZA-15 was dispersed in a 1000 beaker containing MB solution (10 ppm, 625 mL). The reaction was allowed for a 30 min adsorption−desorption process. Then, the reaction took place for 100 min under visible light irradiation, which is the same procedure used for the degradation of MB dye mentioned above. After the first run, the catalyst was recovered from the mixture by centrifugation, washed, and dried before the next cycle was performed. The recovered catalyst was reused in the second run of the photodegradation of MB under a similar procedure. The same procedure was followed for the next run. Then, aliquots were withdrawn after a 100 min reaction for each cycle. Then, the aliquot was centrifuged and analyzed by using a UV−vis spectrophotometer.

3. RESULTS AND DISCUSSION

3.1. Characterization. The phase and crystal structures of the pure ZnO, CZ-1, CZ-2, CZ-3, and CZ-4 samples were examined, and are shown in Figure 1a. The diffraction peaks corresponding to (100), (002), (101), (102), (110), (103), (200), (112), and (201) planes at 2θ values of 33, 35, 36, 48, 57, 63, 68, 70, and 77° matched those of the hexagonal wurtzite structured ZnO (JCPDS no. 036-1451). However, the incorporation of Cu ions caused a marginal shift in the prepared ZnO XRD peaks toward higher angles (Figure 1b). This phenomenon is due to the shrinkage of the ZnO crystal

https://doi.org/10.1021/acsomega.3c08051
ACS Omega 2024, 9, 13714−13727

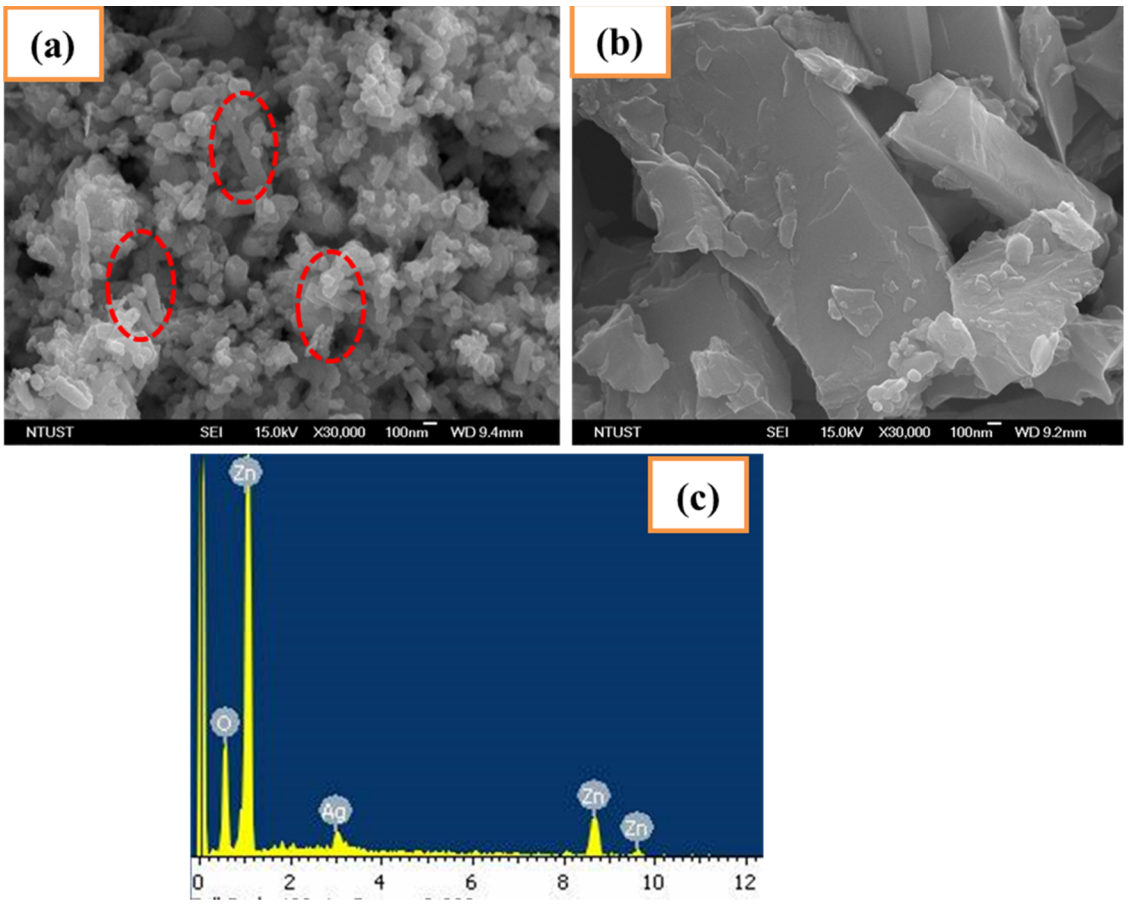

Figure 2. SEM images of CZA-15: (a) templated with cellulose and (b) without cellulose. (c) EDS analysis of the CZA-15 sample templated with cellulose.

lattice as a result of the substitution of Zn^{2+} (0.074 nm) with smaller Cu^{2+} (0.072 nm). The results were also further confirmed with the incorporation of Cu^{2+} into the crystal lattice of ZnO.[44,45] As we have seen from the XRD analysis, there were no additional Cu-related phases in the CZ-1, CZ-2, and CZ-3 samples in which the proper substitution of Zn^{2+} with Cu^{2+} without altering the ZnO lattice structure was successful.[25] However, additional peaks were observed after the addition of an excess amount of Cu (CZ-4). The XRD diffraction peaks corresponding to CuO were observed at 2θ values of 31 and 39°.

Based on the catalytic performance of the $Zn_{1-X}Cu_XO$ samples, 2% Cu-doped ZnO (CZ-2) was used for further deposition of Ag_2O. The XRD diffraction patterns of pure Ag_2O, CZ-2, CZA-10, CZA-15, CZA-30, and CZA-45 samples are shown in Figure 1c. As indicated by the XRD results, the cubic Ag_2O peaks located at 2θ values of 32, 38, 55, and 66° were clearly observed (JCPDS no. 041-1104). It was also demonstrated that there were no phase changes after the deposition of Ag_2O onto Cu-doped ZnO. However, the XRD peaks for Ag_2O were not clearly observed for the CZA-10 and CZA-15 samples, in which the amount of Ag_2O deposited was smaller. Consequently, as the amount of Ag_2O deposited increased (CZA-30 and CZA-45), Ag_2O peaks were clearly observed at 2θ values of 33 and 38°. The results further confirmed that the preparation of the $Zn_{0.98}Cu_{0.02}O/Ag_2O$ nanocomposite catalyst was successful.

The morphologies of the CZA-15 catalysts prepared with and without templated cellulose were examined, as shown in Figure 2a,b, respectively. The SEM images of the CZA-15 catalyst prepared with cellulose as a template showed a representative rod-like structure with smaller sizes (Figure 2a). However, the catalyst synthesized without cellulose as a template showed an agglomerated morphology with large particle sizes (Figure 2b). The results further demonstrated that the utilization of cellulose as a template prevents agglomeration and reduces the particle size to a smaller one. Moreover, energy dispersive X-ray spectroscopy (EDS) analysis also clearly showed representative Zn, Ag, and O elements in the CZA-15 composite catalyst (Figure 2c).

TEM characterization was also performed in order to further examine the morphology of the prepared catalyst. Figure 3a−c shows TEM images of the cellulose-templated CZA-15 catalyst at lower, medium, and higher magnifications, respectively. As indicated by the TEM images, rod-like morphologies were observed, which are also similar to the SEM images in Figure 2a. Moreover, high-resolution TEM (HRTEM) image of the CZA-15 sample was also obtained (Figure 3d). The lattice fringe with a *d*-spacing of 0.26 nm for the (002) plane showed the presence of ZnO in the composite sample. The results also indicated that a good crystalline structure was obtained, which was also confirmed by the XRD analysis shown in Figure 1. However, the lattice fringe for Ag_2O was not clearly observed since the amount of Ag_2O deposited was smaller.

XPS analysis was also conducted to determine the chemical composition of the catalyst. Figure 4a−d shows the XPS spectra of Zn 2p, Ag 3d, Cu 2p, and O 1s peaks. As indicated in Figure 4a, the binding energies of Zn $2p_{3/2}$ and Zn $2p_{1/2}$ at

https://doi.org/10.1021/acsomega.3c08051
ACS Omega 2024, 9, 13714−13727

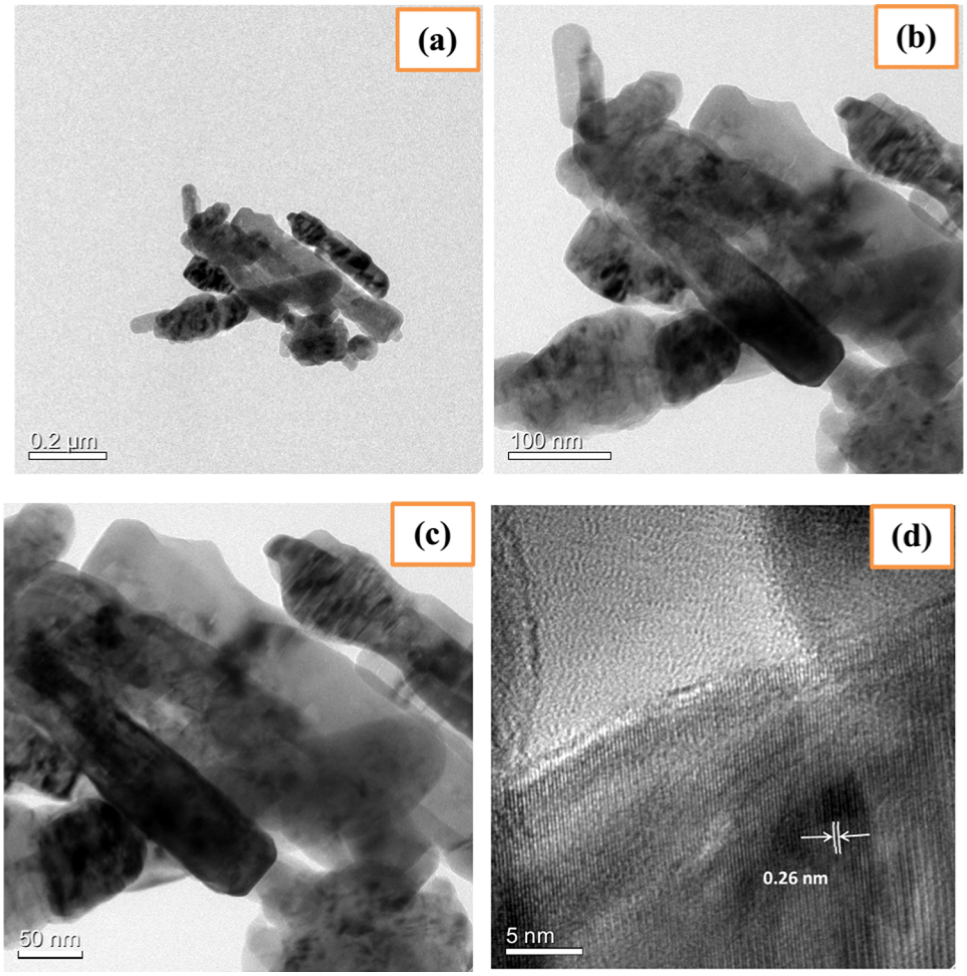

Figure 3. (a–c) TEM images of the cellulose-templated CZA-15 sample at low, medium, and high magnifications. (d) HRTEM image of the cellulose-templated CZA-15 sample.

1022.51 and 1045.60 eV, respectively, were due to the presence of Zn^{2+} in ZnO.[46,47] Moreover, the binding energies of Ag $3d_{5/2}$ and Ag $3d_{1/2}$ at 367.75 and 373.86 eV, respectively, were due to the presence of Ag^{+} in Ag_2O (Figure 4b).[48] The binding energies of Cu $2p_{3/2}$ and Cu $2p_{1/2}$ at 933.60 and 955.42 eV, respectively, showed Cu^{2+} in the composite catalyst.[49] However, the peaks for Cu $2p_{3/2}$ and Cu $2p_{1/2}$ were not intense because the amount of copper ions incorporated into the sample was smaller (Figure 4c). Moreover, Figure 4d indicates the O 1s spectral peaks. The peaks located at binging energies of 530.1, 531.3, and 532.4 eV were ascribed to lattice oxygen, oxygen vacancy, and hydroxyl oxygen, respectively.[30]

FTIR measurements were also performed to identify the functional groups of cellulose and the other prepared samples. The peaks observed at 3442 cm^{-1} indicated the O–H stretching bonds, which may be attributed to the absorbed water and the presence of α-cellulose.[50] The peak at 2908 cm^{-1} for both cellulose (Figure 5a) and CZ-2 (uncalcined) (Figure 5b) samples indicated the presence of C–H stretching in cellulose.[51,52] Moreover, the FTIR peaks located at 1631 cm^{-1} indicated bound H_2O in all samples. Similarly, the C–H and C–O bendings for cellulose are located at 1058 and 1376 cm^{-1}, respectively.[53] Moreover, the peak at 1398 cm^{-1} indicates the Ag_2O vibration in the CZA-15 sample (Figure 5b).[54]

The optical properties of the pure ZnO, Ag_2O, CZ-2, and CZA-15 samples were determined, and are shown in Figure 6. The measurement for pure ZnO showed a higher reflectance, which indicated that it had insignificant absorption in the visible light region.[23] However, CZ-2 showed lower reflectance than ZnO and better absorption in the visible light region. Moreover, the reflectance for CZA-15 was lower than that for both pure ZnO and Cu-doped ZnO samples, which indicated that it could have a higher absorption property in visible light. However, compared to all samples, Ag_2O had a higher absorbance in the visible light region (Figure 6a). Although Ag_2O had higher visible light absorption, the higher electron and hole recombination rates limit its photocatalytic activities.[55] According to the Kubelka–Munk function, the optical band gap values for ZnO, CZ-2, and CZA-15 samples were calculated.[56] The band gap values of pure ZnO, CZ-2, and CZA-15 were 3.21, 3.19, and 2.99 eV, respectively (Figure 6b). These results indicated that the optical band gap shifting was attributed to the induced defects in the Cu-doped ZnO sample.[56] The loading of Ag_2O on Cu-doped ZnO played a significant role in shifting the band gap of Cu-ZnO into the more visible light region (E_g = 3.19 to E_g = 2.99 eV). Furthermore, the band gap for Ag_2O was also calculated as 1.26 eV (Figure 6c). The results further proved that the composite catalyst was successfully synthesized.

https://doi.org/10.1021/acsomega.3c08051
ACS Omega 2024, 9, 13714–13727

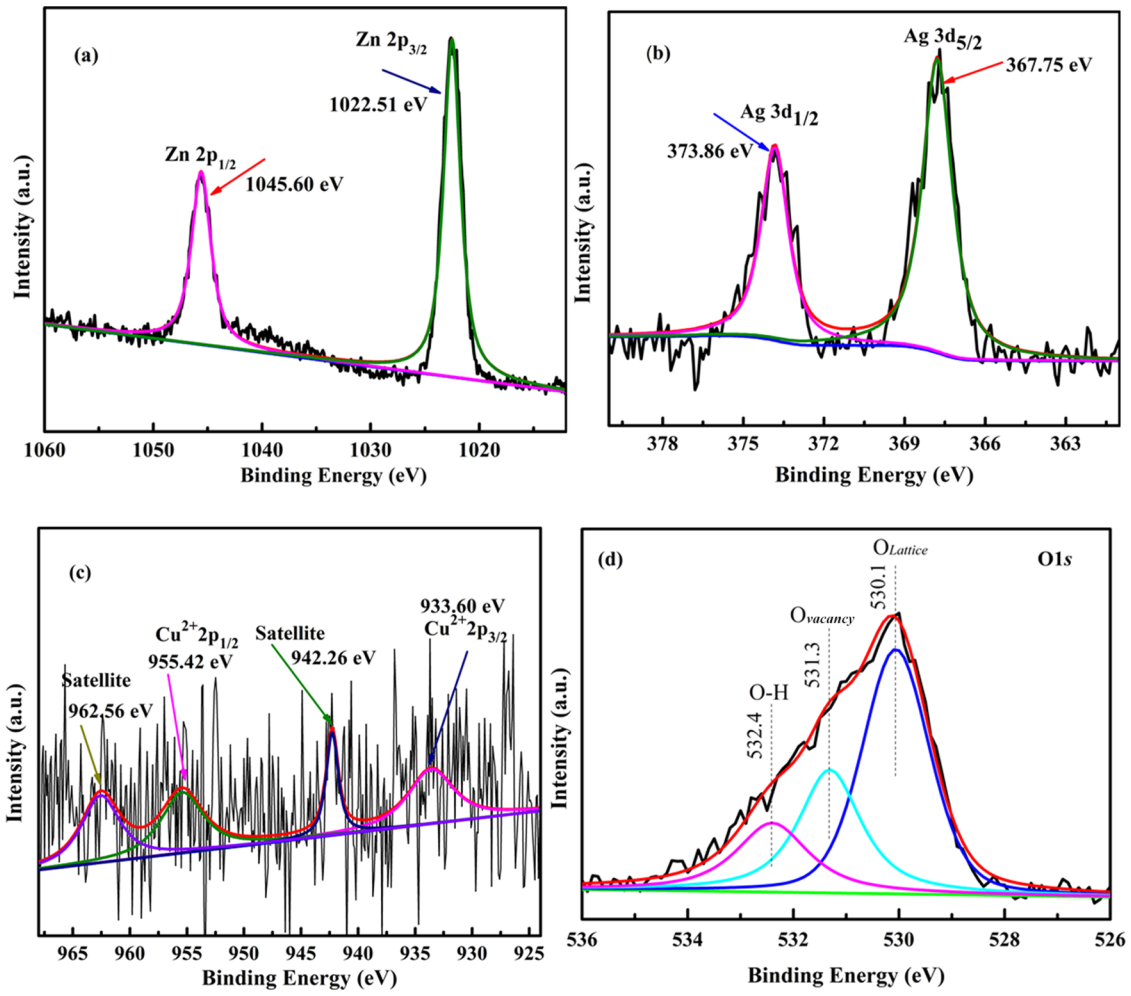

Figure 4. XPS spectra of (a) Zn 2p, (b) Ag 3d, (c) Cu 2p, and (d) O 1s for the cellulose-templated CZA-15 catalyst.

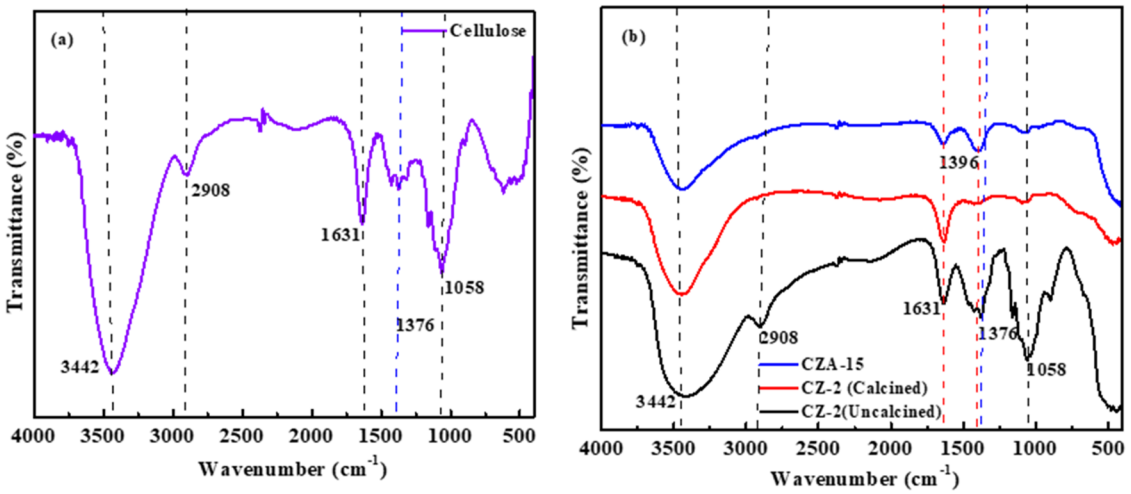

Figure 5. FTIR spectra of (a) cellulose, (b) CZ-2 (uncalcined), CZ-2 (calcined), and CZA-15 samples.

Electrochemical impedance spectroscopy (EIS) measurements were conducted to determine the charge separation efficiencies of the photocatalysts. Figure 6d shows the EIS measurements of the pure ZnO and CZA-15 nanocomposite. As demonstrated by the EIS results, the CZA-15 nanocomposite catalyst had a smaller arc radius. The smaller arc radius of the catalysts resulted in the lowest charge transfer resistance and higher charge transfer rates.[57] The results also further demonstrated that the CZA-15 nanocomposite catalyst had higher charge transfer rates than pure ZnO. This could facilitate hindering the electron and hole recombination rates due to the doping of Cu in the ZnO lattice and the heterojunction formation between ZnO and Ag_2O.

https://doi.org/10.1021/acsomega.3c08051
ACS Omega 2024, 9, 13714−13727

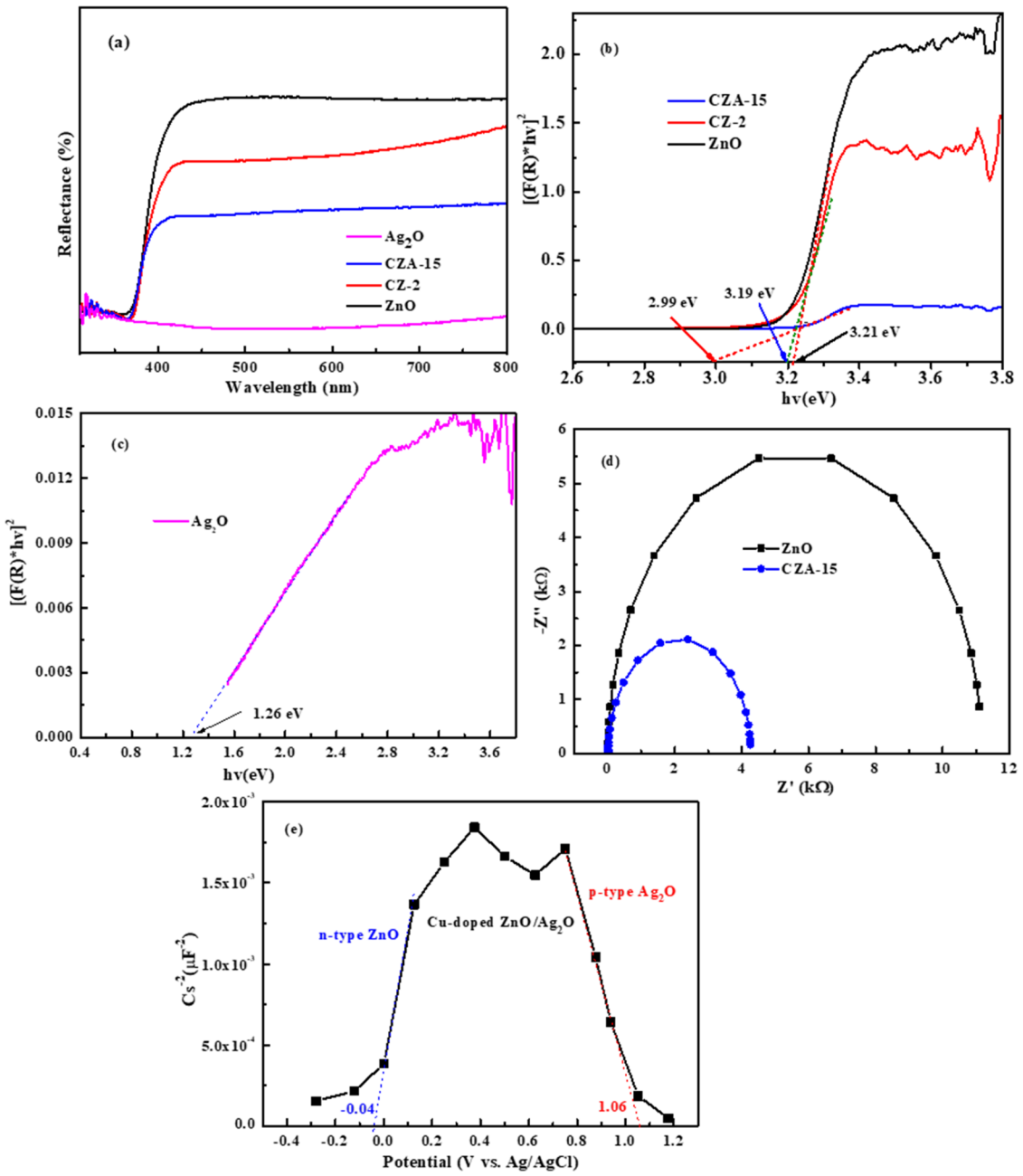

Figure 6. (a) UV−vis absorption for ZnO, CZ-2, CZA-15, and Ag_2O, (b, c) band gap plots for ZnO, CZ-2, CZA-15, and Ag_2O, respectively. (d) EIS plots for ZnO and CZA-15 samples. (e) M−S plot of the CZA-15 sample.

The M−S measurement was performed at 7 kHz to determine the photoinduced charge transfer pathway and the types of semiconductors in the composite catalyst. Figure 6e demonstrates the M−S plots of the CZA-15 composite catalyst. The M−S plot exhibited both a positive and negative slope together, which implies the n-type (ZnO) and p-type (Ag_2O) behavior of semiconductors, respectively.[58] This demonstrates that the successful synthesis of the p−n junction in the $Zn_{0.98}Cu_{0.02}O/Ag_2O$ (CZA-15) composite catalyst was achieved.[59] Moreover, the tangent intercepts of the *x*-axis at −0.04 and +1.06 eV in the composite catalyst represented ZnO and Ag_2O semiconductors, respectively. It is expected that the prepared CZA-15 composite catalyst could have a higher photocatalytic performance than pure ZnO and Ag_2O due to the p-n heterojunction formation and electron and hole separation efficiencies.

3.2. Photocatalytic Activities. To evaluate the photocatalytic performance of the prepared catalysts, MB dye was used as a model organic pollutant. The photocatalytic performance of pure ZnO and Cu-doped ZnO (CZ-1, CZ-2, CZ-3, and CZ-4) was evaluated. Figure 7a shows the change in the concentration of the MB dye at different time intervals in the presence of the CZ-2 catalyst prepared with cellulose as a template. Moreover, Figure 7b shows the C_t/C_0 ratios (where C_0 is the initial concentration and C_t is the concentration of MB at time t (in min)). As indicated in Figure 7b, a higher catalytic efficiency was observed in the presence of CZ-2, which degraded 82% of the MB dye, while pure ZnO, CZ-1, CZ-3, and CZ-4 catalysts degraded 54, 63, 65, and 60% of MB,

https://doi.org/10.1021/acsomega.3c08051
ACS Omega 2024, 9, 13714−13727

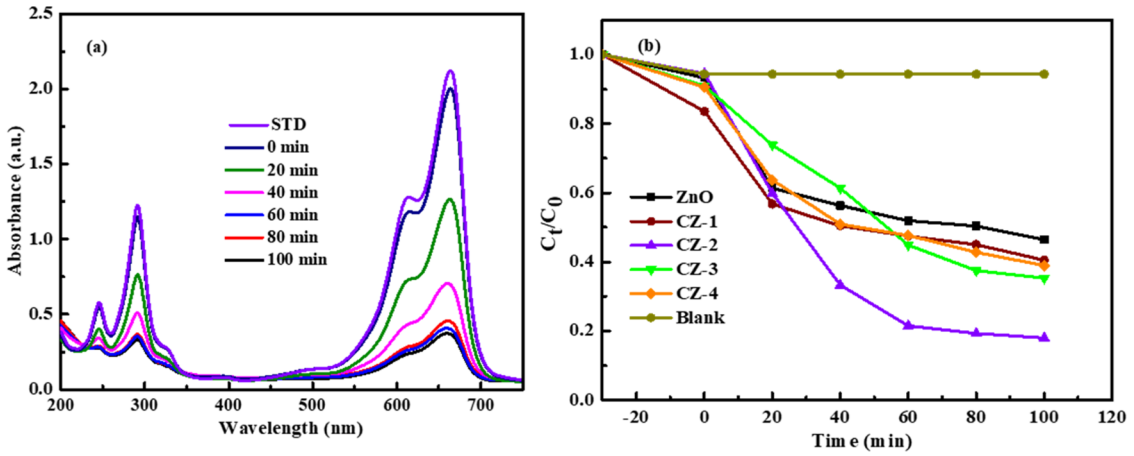

Figure 7. (a) UV−vis absorption spectra of MB degradation with CZ-2, and (b) C_t/C_0 plots for blank (without catalyst) and pure ZnO, CZ-1, CZ-2, CZ-3, and CZ-4 catalysts under visible light irradiation.

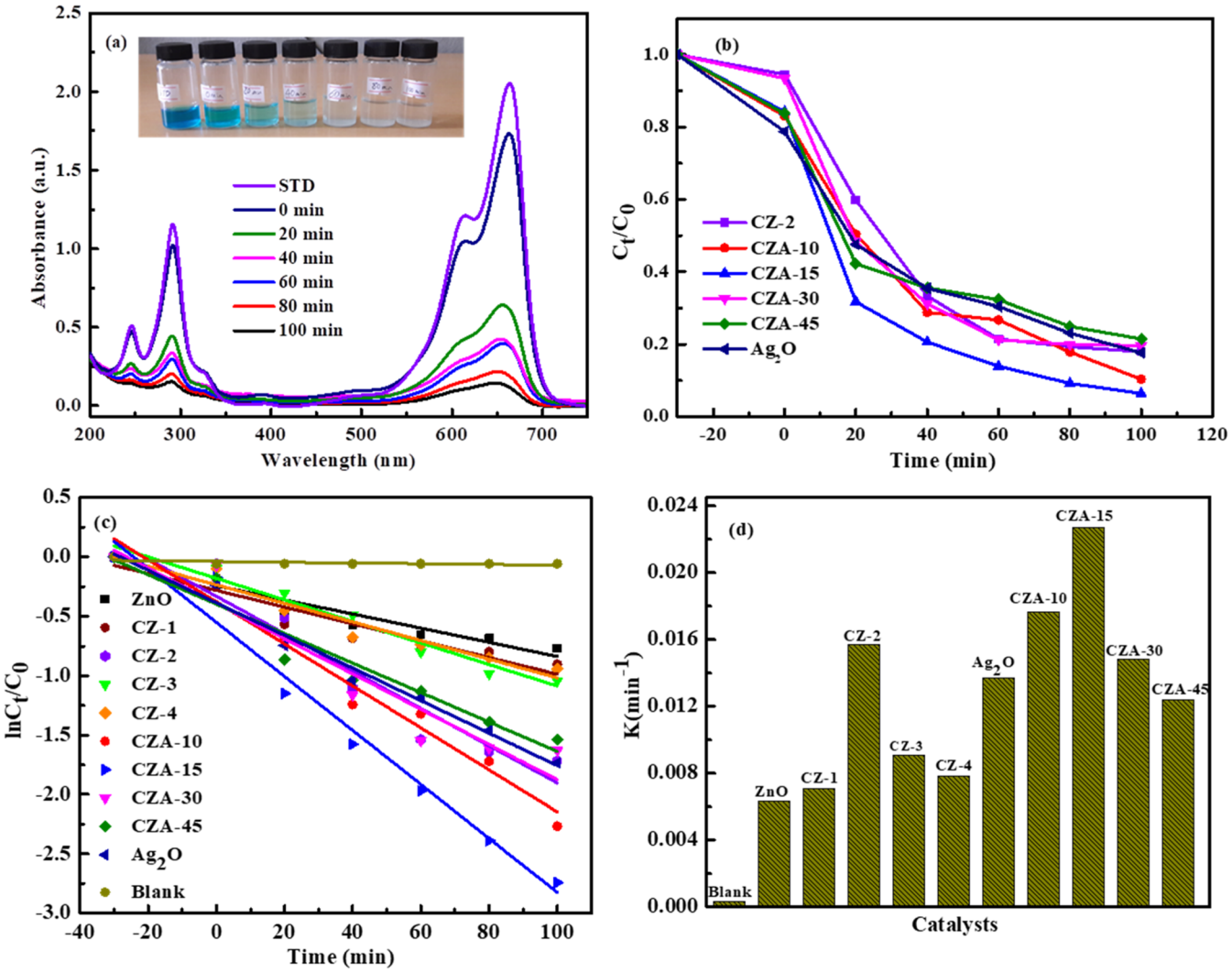

Figure 8. (a) UV−vis absorption spectra of MB degradation with CZA-15. (b) C_t/C_0 plots for CZ-2, CZA-10, CZA-15, CZA-30, CZA-45, and Ag_2O catalysts. (c) The first-order kinetic plot, and (d) the rate constants of blank (without catalyst), ZnO, CZ-1, CZ-2, CZ-3, CZ-4, CZA-10, CZA-15, CZA-30, CZA-45, and Ag_2O catalysts under visible light irradiation.

respectively. However, the degradation of MB without a catalyst was not successful, and only 6% of the dye was degraded within 100 min. The results demonstrate that the incorporation of Cu ions into the ZnO lattice significantly enhanced the catalytic performance. Based on the above considerations, 2% Cu-doped ZnO (CZ-2), which has higher

https://doi.org/10.1021/acsomega.3c08051
ACS Omega 2024, 9, 13714−13727

Table 1. Comparison of the Photocatalytic Degradation Performance of the CZA-15 Photocatalyst with the Other Reported Catalysts

catalysts	catal. (mg)	conc. of MB (ppm)	light	time (min)	deg. (%)	ref
$NiFe_2O_4$/ZnO	50	5	UV	80	91.36	63
ZnO/Bi_2WO_6−CC	10	10	UV	100	96.9	64
Ag/GO/ZnO	300	15	UV	180	85.72	65
ZnO/Ag	70	10	sunlight	120	90.2	66
ZnO-NPs	25	20	UV	140	88	67
Cu-doped ZnO	100	20	sunlight	180	89	68
Cu-doped ZnO	10	10	Vis	100	82	this work
CZA-15	10	10	Vis	10	94	this work

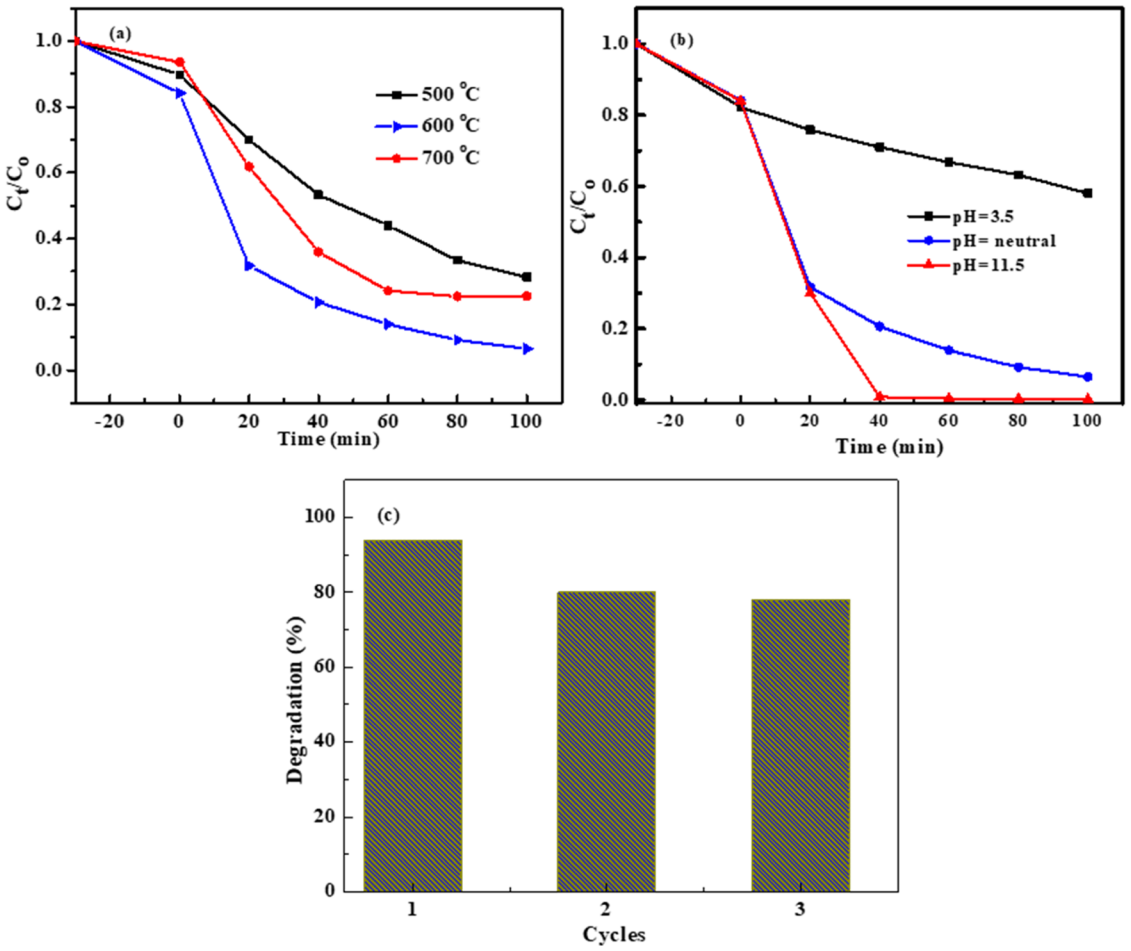

Figure 9. (a, b) Effects of calcination temperature and pH, (c) reusability test for the CZA-15 sample.

catalytic performance, was chosen to further improve the catalytic efficiency.

To further improve the catalytic performance of Cu-doped ZnO (CZ-2), deposition of Ag_2O was performed. Figure 8a shows the change in the concentration of the MB dye at different time intervals in the presence of CZA-15. Here, different amounts of $AgNO_3$ (10, 15, 30, and 45 mg) were used for the deposition of Ag_2O on the surface of CZ-2 and denoted as CZA-10, CZA-15, CZA-30, and CZA-45, respectively. Among the composite catalysts, CZA-15 showed a higher degradation efficiency and degraded 94% of MB, while the CZA-10, CZA-30, and CZA-45 catalysts showed 90, 81, and 79% degradation efficiencies, respectively, under visible light irradiation (Figure 7b). As seen from the data, increasing the Ag_2O content will enhance the catalytic activity toward the degradation of organic pollutants. However, at higher Ag_2O contents, the photocatalytic performance of the catalysts decreased. The results could be due to the full coverage of CZ-2 surfaces with Ag_2O particles.[60] Therefore, CZA-15 (with 10.2% Ag_2O) was the optimum amount of the Ag_2O loaded onto the CZ-2 sample. On the other hand, the photodegradation efficiencies of individual n-type ZnO and p-type Ag_2O oxides were ineffective. However, the Cu-doped ZnO/Ag_2O was much better due to the formation of the p−n junction, which can inhibit the electron−hole recombination rates.[61]

The degradation kinetics curves and the rate constants over different samples for the photocatalytic degradation of MB are shown in Figure 8c,d. The rate expression is given by $\ln (C_t/C_0) = -kt$, where C_t is the concentration at time t, C_0 is the

https://doi.org/10.1021/acsomega.3c08051
ACS Omega 2024, 9, 13714−13727

initial concentration of the MB dye, and k is the apparent first-order rate constant.[48] The photocatalytic degradation reaction showed pseudo-first-order kinetics according to kinetic fitting.[62] The rate constants (k) for blank, ZnO, CZ-1, CZ-2, CZ-3, CZ-4, CZA-10, CZA-15, CZA-30, CZA-45, and Ag_2O catalysts were found to be 0.00032, 0.0063, 0.007, 0.016, 0.009, 0.008, 0.018, 0.023, 0.015, 0.012, and 0.014 min^{-1}, respectively. The highest kinetic rate was found to be 0.023 min^{-1} for the CZA-15 sample. The results confirmed that the photodegradation efficiency of the CZA-15 composite was much higher than those of the individual ZnO and Ag_2O photocatalysts under visible light irradiation. The catalytic efficiency of the $Zn_{0.98}Cu_{0.02}O/Ag_2O$ (CZA-15) composite catalyst was also compared with those previously reported. As demonstrated in Table 1, our catalyst system is comparable with those reported in the literature.

The effect of calcination temperature on the CZ-2 catalyst was also optimized, as shown in Figure 9a. The photocatalytic performance of cellulose-templated metal oxide heterostructures mainly depends on the calcination temperature at which the cellulose is burned out and removed from the synthesized metal oxide heterostructure.[38] The photocatalytic degradation efficiency of the CZA-15 catalyst calcined at 500, 600, and 700 °C was tested for MB degradation under visible light illumination. The catalyst calcined at 600 °C showed a higher photocatalytic performance and degraded 94% of the MB dye, while the photocatalytic performance at calcination temperatures of 500 and 700 °C decreased and showed 72 and 78% degradation efficiencies, respectively. The higher photocatalytic degradation calcined at 600 °C may be due to defects and the higher active sites of the semiconductor.[69] Moreover, the lower catalytic activity at 500 °C could be due to the fact that most of the carbon-based polymeric structures may not be removed at relatively low temperatures.[70] On the other hand, at relatively high temperatures (700 °C), the porosity will be narrowed as they are ceramics, and may be a decrease of active sites owing to diminished surface areas.[71]

The pH of the solution is also a key factor for the photocatalytic degradation reaction.[72] The catalytic performance at neutral pH had a 94% degradation efficiency (Figure 9b). However, in basic media (pH = 11.5), complete degradation of the MB dye was achieved within 40 min of irradiation, while only 42% of MB degradation was achieved within 100 min of irradiation in acidic media (pH = 3.5) with the CZA-15 catalyst. According to previous reports, when the pH of the dye solution became more basic, the surface tends to acquire a negative charge, thereby resulting in increased adsorption of dyes because of the increasing electrostatic attraction between the positively charged dye and the negatively charged catalyst.[73]

The reusability of the CZA-15 composite photocatalyst was also investigated with three consecutive tests within 100 min under visible light irradiation. As demonstrated in Figure 9c, the CZA-15 composite catalyst remained active after three consecutive reactions and degraded 78% of the MB dye. Therefore, the CZA-15 composite catalyst is a promising photocatalyst that can be useful for wastewater treatment applications.

3.3. Photocatalytic Degradation Mechanism. Based on the above characterization results and literature reports, a possible photodegradation mechanism for MB dye degradation was demonstrated, as shown in Figure 10. To deduce the degradation mechanism of the organic dye, the energy levels of

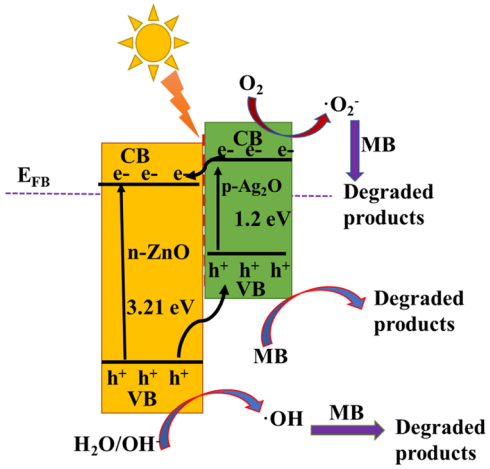

Figure 10. Schematic diagram for the degradation mechanism of MB using the $Zn_{0.98}Cu_{0.02}O/Ag_2O$ catalyst.

ZnO and Ag_2O are required. As demonstrated, ZnO is an n-type semiconductor with a wide band gap, while Ag_2O is a p-type semiconductor with a narrow band gap.[29] Moreover, the VB and CB of ZnO and Ag_2O can be estimated theoretically by Mulliken's empirical equations[74]

$$E_{VB} = 0.5E_g + x - E_e \quad (1)$$

$$E_{CB} = E_{VB} - E_g \quad (2)$$

where χ is the Pearson electronegativity, E_g is the optical band gap energy, and E_e is the free electron energy (4.5 eV). The χ values for ZnO and Ag_2O are ~5.79 and 5.29 eV, respectively.[74] Therefore, the calculated E_{VB} and E_{CB} values for ZnO are 2.90 and −0.32 eV, while the E_{VB} and E_{CB} values for Ag_2O are 1.42 and 0.16 eV, respectively.

According to the calculated results mentioned above, the photocatalytic degradation mechanism of MB under visible light irradiation with a $Zn_{0.98}Cu_{0.02}O/Ag_2O$ (CZA-15) composite catalyst is demonstrated and shown in Figure 10. The electron transfer from the VB to the CB of ZnO is not easy under visible light irradiation due to the large band gap energy of ZnO (3.21 eV). Moreover, the Fermi level in pre-equilibrium for the n-ZnO and p-Ag_2O semiconductors was exhibited at different positions. According to the formation theory of the p−n heterojunction, the Fermi level of n-type ZnO is moved down while the Fermi level of p-type Ag_2O is moved up until an equilibrium state is formed.[75] In the photocatalysis process, the electrons can be transferred from n-ZnO to the p-Ag_2O semiconductor until the system reaches equilibrium through Fermi-level alignment.[61] Moreover, the carrier concentration gradients were formed, and a built-in electric field at the p-Ag_2O/n-ZnO heterojunctions.[76] At equilibrium, the p-type Ag_2O semiconductor has a negative charge at the junction, while the n-type ZnO semiconductor has a positive charge. This results in the transfer of holes from the VB of ZnO to the Ag_2O region, while the electrons from the CB of Ag_2O to the ZnO region are due to the internal electric field.[77] The p−n heterojunction formation and electron transfer efficiencies of the CZA-15 composite catalyst were also proved from the M−S plot (Figure 6e) and EIS measurements (Figure 6c), respectively.

During the transfer of the photogenerated e^- to the Ag^+ sites in the photocatalysis system, in situ partial reduction of Ag_2O

https://doi.org/10.1021/acsomega.3c08051
ACS Omega 2024, 9, 13714−13727

to metallic Ag^0 occurs on the surface of Ag_2O. The photogenerated e^- accumulation on the surface of the Ag^0 can reduce O_2 to $^{\bullet}O_2^-$ ($O_2 + e^- = {}^{\bullet}O_2^-$, −0.046 eV vs NHE).[78] Moreover, the holes in the VB of Ag_2O cannot oxidize H_2O or OH^- to produce $^{\bullet}OH$ since the Ag_2O redox potential (1.42 V vs NHE) is less positive than that of the $H_2O/{}^{\bullet}OH$ (+2.72 eV) and $OH^-/{}^{\bullet}OH$ (+2.69 eV) to produce $^{\bullet}OH$. Therefore, the holes in the VB of Ag_2O can directly oxidize the MB dye. Similarly, since the redox potential of ZnO (2.90 V vs NHE) is more positive than that of $H_2O/{}^{\bullet}OH$ (+2.72 eV) and $OH^-/{}^{\bullet}OH$ (+2.69 eV), it can produce $^{\bullet}OH$.[79] Therefore, h^+, $^{\bullet}OH$, and $^{\bullet}O_2^-$ are active species for the degradation of organic pollutants.[80]

4. CONCLUSIONS

Herein, cellulose-templated Cu-doped ZnO catalysts with different amounts of Cu dopants were prepared and tested for the degradation of MB. Among the prepared catalysts, 2% Cu-doped ZnO (CZ-2) showed the best catalytic performance and degraded 82% of the MB dye, while pure ZnO degraded only 54% of the MB dye. The CZ-2 photocatalytic efficiency was also further improved by the deposition of an optimum amount of Ag_2O, and the $Zn_{0.98}Cu_{0.02}O/Ag_2O$ (CZA-15) nanocomposite catalyst degraded 94% of the MB dye. The results demonstrated that Cu-doping with an optimum amount into the ZnO lattice followed by p−n junction formation between Ag_2O and ZnO further improved the catalytic performance. The higher photocatalytic efficiencies of the CZA-15 nanocomposite catalysts could be due to an increase in the number of active sites, inhibition of the electron and hole recombination rates, higher charge transfer efficiency, and higher visible light absorption properties of the catalyst. Therefore, a cellulose-templated catalyst with an optimum amount of Cu-doped ZnO and further deposition with an optimum amount of Ag_2O on the surface of Cu-doped ZnO could have promising applications in the degradation of organic pollutants.

AUTHOR INFORMATION

Corresponding Author

Osman Ahmed Zelekew − *Department of Materials Science and Engineering, Adama Science and Technology University, Adama 1888, Ethiopia;* orcid.org/0000-0003-2633-5426; Email: osmanx2007@gmail.com, osman.ahmed@astu.edu.et

Authors

Biruktait Ayele Lemecho − *Department of Materials Science and Engineering, Adama Science and Technology University, Adama 1888, Ethiopia*

Dinsefa Mensur Andoshe − *Department of Materials Science and Engineering, Adama Science and Technology University, Adama 1888, Ethiopia;* orcid.org/0000-0001-9664-1344

Noto Susanto Gultom − *Department of Materials Science and Engineering, National Taiwan University of Science and Technology, Taipei 10607, Taiwan;* orcid.org/0000-0001-5418-4296

Hairus Abdullah − *Department of Materials Science and Engineering, National Taiwan University of Science and Technology, Taipei 10607, Taiwan;* orcid.org/0000-0002-1775-535X

Dong-Hau Kuo − *Department of Materials Science and Engineering, National Taiwan University of Science and Technology, Taipei 10607, Taiwan;* orcid.org/0000-0001-9300-8551

Xiaoyun Chen − *College of Materials Engineering, Fujian Agriculture and Forestry University, Fuzhou 350002, China;* orcid.org/0000-0002-3973-7726

Temesgen D. Desissa − *Department of Materials Science and Engineering, Adama Science and Technology University, Adama 1888, Ethiopia*

Demeke Tesfaye Wondimageng − *Department of Materials Science and Engineering, Adama Science and Technology University, Adama 1888, Ethiopia*

Yi-nan Wu − *College of Environmental Science and Engineering, State Key Laboratory of Pollution Control and Resource Reuse, Tongji University, Shanghai 200092, China; Shanghai Institute of Pollution Control and Ecological Security, Shanghai 200092, China;* orcid.org/0000-0001-6703-019X

Complete contact information is available at: https://pubs.acs.org/10.1021/acsomega.3c08051

Notes

The authors declare no competing financial interest.

ACKNOWLEDGMENTS

This MSc. thesis work was supported by the Adama Science and Technology University (ASTU) under grant No. ASTU/SM-R/125/19. We also acknowledge the National Taiwan University of Science and Technology (NTUST) for SEM, TEM, and XPS analyses.

REFERENCES

(1) Chen, L.; Su, Z.; Wu, Q.; Kuo, D.-H.; Abdeta, A. B.; Wu, B.; Zhang, P.; Mosisa, M. T.; Zelekew, O. A.; Lin, J.; Chen, X.; Liu, X. Co/S co-doped Mn3O4-based sulfur-oxide nano-flakes catalyst for highly efficient catalytic reduction of organics and hexavalent chromium pollutants. *J. Water Process Eng.* **2023**, *55*, No. 104168.

(2) Fan, Y.; Fang, C. A comprehensive insight into water pollution and driving forces in Western China—case study of Qinghai. *J. Cleaner Prod.* **2020**, *274*, No. 123950.

(3) Zelekew, O. A.; Kuo, D.-H. Synthesis of a hierarchical structured NiO/NiS composite catalyst for reduction of 4-nitrophenol and organic dyes. *RSC Adv.* **2017**, *7* (8), 4353−4362.

(4) Yin, L.; Wang, D.; Li, X.; He, Y.; Liu, X.; Xu, Y.; Chen, H. One-pot synthesis of oxygen-vacancy-rich Cu-doped UiO-66 for collaborative adsorption and photocatalytic degradation of ciprofloxacin. *Sci. Total Environ.* **2022**, *815*, No. 151962.

(5) Chen, X.; Sun, H.; Zelekew, O. A.; Zhang, J.; Guo, Y.; Zeng, A.; Kuo, D.-H.; Lin, J. Biological renewable hemicellulose-template for synthesis of visible light responsive sulfur-doped TiO2 for photocatalytic oxidation of toxic organic and As(III) pollutants. *Appl. Surf. Sci.* **2020**, *525*, No. 146531.

(6) Li, P.; Wu, Q.; Ji, Q.; Abdeta, A. B.; Kuo, D.-H.; Huang, T.; Zhang, H.; Zelekew, O. A.; Lin, J.; Chen, X. Sulfur-doped Sb4Mo10O31 bimetallic sulfur-oxide catalyst for highly efficient reduction of toxic organic and hexavalent chromium under dark. *J. Environ. Chem. Eng.* **2023**, *11* (5), No. 110700.

(7) Barisci, S.; Suri, R. Electrooxidation of short and long chain perfluorocarboxylic acids using boron doped diamond electrodes. *Chemosphere* **2020**, *243*, No. 125349.

(8) Priyadarshini, M.; Das, I.; Ghangrekar, M. M.; Blaney, L. Advanced oxidation processes: Performance, advantages, and scale-up of emerging technologies. *J. Environ. Manage.* **2022**, *316*, No. 115295.

(9) Bora, L. V.; Mewada, R. K. Visible/solar light active photocatalysts for organic effluent treatment: Fundamentals, mech-

https://doi.org/10.1021/acsomega.3c08051
ACS Omega 2024, 9, 13714−13727

anisms and parametric review. *Renewable Sustainable Energy Rev.* **2017**, *76*, 1393−1421.
(10) Babuponnusami, A.; Muthukumar, K. A review on Fenton and improvements to the Fenton process for wastewater treatment. *J. Environ. Chem. Eng.* **2014**, *2* (1), 557−572.
(11) Gogate, P. R.; Pandit, A. B. A review of imperative technologies for wastewater treatment I: oxidation technologies at ambient conditions. *Adv. Environ. Res.* **2004**, *8* (3−4), 501−551.
(12) Gogate, P. R.; Pandit, A. B. A review of imperative technologies for wastewater treatment II: hybrid methods. *Adv. Environ. Res.* **2004**, *8* (3−4), 553−597.
(13) Andreozzi, R.; Caprio, V.; Insola, A.; Marotta, R. Advanced oxidation processes (AOP) for water purification and recovery. *Catal. Today* **1999**, *53* (1), 51−59.
(14) Ao, D.; Zhang, J.; Liu, H. Visible-light-driven photocatalytic degradation of pollutants over Cu-doped NH2-MIL-125(Ti). *J. Photochem. Photobiol., A* **2018**, *364*, 524−533.
(15) Zhu, S.; Wang, D. Photocatalysis: Basic Principles, Diverse Forms of Implementations and Emerging Scientific Opportunities. *Adv. Energy Mater.* **2017**, *7* (23), No. 1700841.
(16) Choe, H.; Kim, S. Y.; Zhao, S.; Cha, B. J.; Grehl, T.; Brüner, P.; Kim, Y. D. Surface Structures of Fe−TiO2 Photocatalysts for NO Oxidation. *ACS Appl. Mater. Interfaces* **2022**, *14* (20), 24028−24038.
(17) Nawaz, A.; Goudarzi, S.; Asghari, M. A.; Pichiah, S.; Selopal, G. S.; Rosei, F.; Wang, Z. M.; Zarrin, H. Review of Hybrid 1D/2D Photocatalysts for Light-Harvesting Applications. *ACS Appl. Nano Mater.* **2021**, *4* (11), 11323−11352.
(18) Liu, S.; Zhou, X.; Yang, C.; Wei, C.; Hu, Y. Cu atoms on UiO-66-NH2/ZnIn2S4 nanosheets enhance photocatalytic performance for recovering hydrogen energy from organic wastewater treatment. *Appl. Catal., B* **2023**, *330*, No. 122572.
(19) Batool, M.; Nazar, M. F.; Awan, A.; Tahir, M. B.; Rahdar, A.; Shalan, A. E.; Lanceros-Méndez, S.; Zafar, M. N. Bismuth-based heterojunction nanocomposites for photocatalysis and heavy metal detection applications. *Nano-Struct. Nano-Objects* **2021**, *27*, No. 100762.
(20) Tan, S. T.; Ali Umar, A.; Salleh, M. M. (001)-Faceted hexagonal ZnO nanoplate thin film synthesis and the heterogeneous catalytic reduction of 4-nitrophenol characterization. *J. Alloys Compd.* **2015**, *650*, 299−304.
(21) Fufa, P. A.; Feysia, G. B.; Gultom, N. S.; Kuo, D.-H.; Chen, X.; Kabtamu, D. M.; Zelekew, O. A. Visible light-driven photocatalytic activity of Cu2O/ZnO/Kaolinite-based composite catalyst for the degradation of organic pollutant. *Nanotechnology* **2022**, *33* (31), No. 315601.
(22) Haitosa, H. H.; Tesfamariam, B. B.; Gultom, N. S.; Kuo, D.-H.; Chen, X.; Wu, Y.-n.; Zelekew, O. A. Stephania abyssinica leaf extract mediated (Mn, Ni) co-doped ZnO catalyst synthesis for the degradation of organic dye. *J. Mol. Liq.* **2022**, *368*, No. 120666.
(23) Vaiano, V.; Iervolino, G.; Rizzo, L. Cu-doped ZnO as efficient photocatalyst for the oxidation of arsenite to arsenate under visible light. *Appl. Catal., B* **2018**, *238*, 471−479.
(24) Yang, H.; Gao, J.; Yang, M.; Hou, H.; Gao, F.; Luo, Y.; Yang, W. One-Pot MOFs-Encapsulation Derived In-Doped ZnO@In2O3 Hybrid Photocatalyst for Enhanced Visible-Light-Driven Photocatalytic Hydrogen Evolution. *Adv. Sustainable Syst.* **2023**, *7* (4), No. 2200443.
(25) Kuriakose, S.; Satpati, B.; Mohapatra, S. Highly efficient photocatalytic degradation of organic dyes by Cu doped ZnO nanostructures. *Phys. Chem. Chem. Phys.* **2015**, *17* (38), 25172−25181.
(26) Bekru, A. G.; Tufa, L. T.; Zelekew, O. A.; Goddati, M.; Lee, J.; Sabir, F. K. Green Synthesis of a CuO−ZnO Nanocomposite for Efficient Photodegradation of Methylene Blue and Reduction of 4-Nitrophenol. *ACS Omega* **2022**, *7* (35), 30908−30919.
(27) Kumari, V.; Yadav, S.; Jindal, J.; Sharma, S.; Kumari, K.; Kumar, N. Synthesis and characterization of heterogeneous ZnO/CuO hierarchical nanostructures for photocatalytic degradation of organic pollutant. *Adv. Powder Technol.* **2020**, *31* (7), 2658−2668.
(28) Aragaw, S. G.; Sabir, F. K.; Andoshe, D. M.; Zelekew, O. A. Green synthesis of p-Co3O4/n-ZnO composite catalyst with Eichhornia Crassipes plant extract mediated for methylene blue degradation under visible light irradiation. *Mater. Res. Express* **2020**, *7* (9), No. 095508.
(29) Sahu, P.; Das, D. Two-Step Visible Light Photocatalytic Dye Degradation Phenomena in Ag2O-Impregnated ZnO Nanorods via Growth of Metallic Ag and Formation of ZnO/Ag0/Ag2O Heterojunction Structures. *Langmuir* **2022**, *38* (15), 4503−4520.
(30) Chen, X.; Sun, H.; Zhang, J.; Ahmed Zelekew, O.; Lu, D.; Kuo, D.-H.; Lin, J. Synthesis of visible light responsive iodine-doped mesoporous TiO2 by using biological renewable lignin as template for degradation of toxic organic pollutants. *Appl. Catal., B* **2019**, *252*, 152−163.
(31) Zelekew, O. A.; Haitosa, H. H.; Chen, X.; Wu, Y.-N. Recent progress on plant extract-mediated biosynthesis of ZnO-based nanocatalysts for environmental remediation: Challenges and future outlooks. *Adv. Colloid Interface Sci.* **2023**, *317*, No. 102931.
(32) Cai, A.; Guo, A.; Du, L.; Qi, Y.; Wang, X. Leaf-templated synthesis of hierarchical AgCl-Ag-ZnO composites with enhanced visible-light photocatalytic activity. *Mater. Res. Bull.* **2018**, *103*, 225−233.
(33) Shi, C.; Zhang, L.; Shi, Z.; Ma, J.; Wang, Z. Cellulose template designed porous ZnO based catalysts with different valence copper for solar photocatalytic CO2 conversion. *Ind. Crops Prod.* **2022**, *186*, No. 115223.
(34) Li, X.; Zhang, L.; Wang, Z.; Wu, S.; Ma, J. Cellulose controlled zinc oxide nanoparticles with adjustable morphology and their photocatalytic performances. *Carbohydr. Polym.* **2021**, *259*, No. 117752.
(35) Wang, H.; Qiu, X.; Liu, W.; Yang, D. Facile preparation of well-combined lignin-based carbon/ZnO hybrid composite with excellent photocatalytic activity. *Appl. Surf. Sci.* **2017**, *426*, 206−216.
(36) Zhang, B.; Yang, D.; Qiu, X.; Qian, Y.; Wang, H.; Yi, C.; Zhang, D. Fabricating ZnO/lignin-derived flower-like carbon composite with excellent photocatalytic activity and recyclability. *Carbon* **2020**, *162*, 256−266.
(37) Malekkiani, M.; Heshmati Jannat Magham, A.; Ravari, F.; Dadmehr, M. Facile fabrication of ternary MWCNTs/ZnO/Chitosan nanocomposite for enhanced photocatalytic degradation of methylene blue and antibacterial activity. *Sci. Rep.* **2022**, *12* (1), No. 5927.
(38) Lin, Z.; Lu, Y.; Huang, J. A hierarchical Ag2O-nanoparticle/TiO2-nanotube composite derived from natural cellulose substance with enhanced photocatalytic performance. *Cellulose* **2019**, *26* (11), 6683−6700.
(39) Kale, G.; Arbuj, S.; Kawade, U.; Kadam, S.; Nikam, L.; Kale, B. Paper templated synthesis of nanostructured Cu−ZnO and its enhanced photocatalytic activity under sunlight. *J. Mater. Sci.: Mater. Electron.* **2019**, *30* (7), 7031−7042.
(40) Guna, V.; Ilangovan, M.; Anantha Prasad, M. G.; Reddy, N. Water Hyacinth: A Unique Source for Sustainable Materials and Products. *ACS Sustainable Chem. Eng.* **2017**, *5* (6), 4478−4490.
(41) Jones, J. L.; Jenkins, R. O.; Haris, P. I. Extending the geographic reach of the water hyacinth plant in removal of heavy metals from a temperate Northern Hemisphere river. *Sci. Rep.* **2018**, *8* (1), 11071.
(42) Istirokhatun, T.; Rokhati, N.; Rachmawaty, R.; Meriyani, M.; Priyanto, S.; Susanto, H. Cellulose Isolation from Tropical Water Hyacinth for Membrane Preparation. *Procedia Environ. Sci.* **2015**, *23*, 274−281.
(43) Perillo, P. M.; Atia, M. N. Solar-assisted photodegradation of methyl orange using Cu-doped ZnO nanorods. *Mater. Today Commun.* **2018**, *17*, 252−258.
(44) Meshram, S. P.; Adhyapak, P. V.; Amalnerkar, D. P.; Mulla, I. S. Cu doped ZnO microballs as effective sunlight driven photocatalyst. *Ceram. Int.* **2016**, *42* (6), 7482−7489.
(45) Babu, B.; Aswani, T.; Rao, G. T.; Stella, R. J.; Jayaraja, B.; Ravikumar, R. Room temperature ferromagnetism and optical properties of Cu2+ doped ZnO nanopowder by ultrasound assisted

https://doi.org/10.1021/acsomega.3c08051
ACS Omega 2024, 9, 13714−13727

solid state reaction technique. *J. Magn. Magn. Mater.* **2014**, *355*, 76−80.
(46) Ahmad, I.; Shoaib Akhtar, M.; Ahmed, E.; Ahmad, M.; Keller, V.; Qamar Khan, W.; Khalid, N. R. Rare earth co-doped ZnO photocatalysts: Solution combustion synthesis and environmental applications. *Sep. Purif. Technol.* **2020**, *237*, No. 116328.
(47) Mar, L. G.; Timbrell, P. Y.; Lamb, R. N. An XPS study of zinc oxide thin film growth on copper using zinc acetate as a precursor. *Thin Solid Films* **1993**, *223* (2), 341−347.
(48) Zelekew, O. A.; Kuo, D.-H.; Yassin, J. M.; Ahmed, K. E.; Abdullah, H. Synthesis of efficient silica supported TiO2/Ag2O heterostructured catalyst with enhanced photocatalytic performance. *Appl. Surf. Sci.* **2017**, *410*, 454−463.
(49) Rajendran, S.; Pachaiappan, R.; Hoang, T. K. A.; Karthikeyan, S.; Gnanasekaran, L.; Vadivel, S.; Soto-Moscoso, M.; Gracia-Pinilla, M. A. CuO-ZnO-PANI a lethal p-n-p combination in degradation of 4-chlorophenol under visible light. *J. Hazard. Mater.* **2021**, *416*, No. 125989.
(50) Prithivirajan, R.; Balasundar, P.; Shyamkumar, R.; Al-Harbi, N. S.; Kadaikunnan, S.; Ramkumar, T.; Narayanasamy, P. Characterization of cellulosic fibers from Morus alba L. stem. *J. Nat. Fibers* **2019**, *16* (4), 503−511.
(51) Vijay, R.; Singaravelu, D. L.; Vinod, A.; Sanjay, M.; Siengchin, S.; Jawaid, M.; Khan, A.; Parameswaranpillai, J. Characterization of raw and alkali treated new natural cellulosic fibers from Tridax procumbens. *Int. J. Biol. Macromol.* **2019**, *125*, 99−108.
(52) Rafique, S.; Kasi, A. K.; Kasi, J. K.; Aminullah; Bokhari, M.; Shakoor, Z. Fabrication of silver-doped zinc oxide nanorods piezoelectric nanogenerator on cotton fabric to utilize and optimize the charging system. *Nanomater. Nanotechnol.* **2020**, *10*, No. 1847980419895741.
(53) Asrofi, M.; Abral, H.; Kasim, A.; Pratoto, A. XRD and FTIR Studies of Nanocrystalline Cellulose from Water Hyacinth (*Eichornia crassipes*) Fiber. *J. Metastable Nanocryst. Mater.* **2017**, *29*, 9−16.
(54) Nguyen, T. T.; Nguyen Thi, Q. A.; Le, N. H.; Nguyen, N. H. Synthesis of a novel porous Ag2O nanomaterial on ion exchange resin and its application for COD determination of high salinity water. *Sci. Rep.* **2021**, *11* (1), No. 11487.
(55) Zhou, P.; Chen, F.; Su, X.; Zhang, T.; Meng, S.; Xie, M.; Song, Y.; Yan, X.; Xu, Y. Ag2O modified magnetic BaFe12O19/C3N4 photocatalysts with enhanced antibiotic removal: Photocatalytic mechanism and toxicity evaluation. *Adv. Powder Technol.* **2023**, *34* (6), No. 104015.
(56) Banu Bahşi, Z.; Oral, A. Y. Effects of Mn and Cu doping on the microstructures and optical properties of sol−gel derived ZnO thin films. *Opt. Mater.* **2007**, *29* (6), 672−678.
(57) Chen, X.; Wu, Q.; Kuo, D.-H.; Abdeta, A. B.; Zhang, H.; Li, P.; Huang, T.; Zelekew, O. A.; Lin, J. Initiating highly efficient (Bi,Ce)2(O,S)3−x oxysulfide catalysts with rich oxygen vacancies for hydrogen evolution via adjusting valence band configuration. *J. Mater. Chem. A* **2023**, *11* (8), 4126−4141.
(58) Chen, Y.; Zhu, G.; Hojamberdiev, M.; Gao, J.; Zhu, R.; Wang, C.; Wei, X.; Liu, P. Three-dimensional Ag2O/Bi5O7I p−n heterojunction photocatalyst harnessing UV−vis−NIR broad spectrum for photodegradation of organic pollutants. *J. Hazard. Mater.* **2018**, *344*, 42−54.
(59) Song, M.; Qi, K.; Wen, Y.; Zhang, X.; Yuan, Y.; Xie, X.; Wang, Z. Rational design of novel three-dimensional reticulated Ag2O/ZnO Z-scheme heterojunction on Ni foam for promising practical photocatalysis. *Sci. Total Environ.* **2021**, *793*, No. 148519.
(60) He, J.; Fu, H.; Wu, P.; Lin, Z.; Zeng, Y.; Jiang, W. Performance Promotion of Ag2O Photocatalyst by Particle Size and Crystal Surface Regulation. *New J. Chem.* **2020**, *44* (25), 10719−10728.
(61) Kadam, A.; Dhabbe, R.; Gophane, A.; Sathe, T.; Garadkar, P. K. M. Template free synthesis of ZnO/Ag2O nanocomposites as a highly efficient visible active photocatalyst for detoxification of Methyl Orange. *J. Photochem. Photobiol., B* **2016**, *154*, 24−33.
(62) Wang, Y.; Liu, L.; Xu, L.; Cao, X.; Li, X.; Huang, Y.; Meng, C.; Wang, Z.; Zhu, W. Ag2O/TiO2/V2O5 one-dimensional nano-heterostructures for superior solar light photocatalytic activity. *Nanoscale* **2014**, *6* (12), 6790−6797.
(63) Tripta; Rana, P. S. NiFe2O4/ZnO nanocomposites for degradation of MB dye with their local electrical behavior. *J. Mol. Struct.* **2023**, *1282*, No. 135160.
(64) Chen, X.; Li, J.; Chen, F. Photocatalytic degradation of MB by novel and environmental ZnO/Bi2WO6-CC hierarchical heterostructures. *Mater. Charact.* **2022**, *189*, No. 111961.
(65) Rashid Al-Mamun, M.; Shofikul Islam, M.; Rasel Hossain, M.; Kader, S.; Shahinoor Islam, M.; Zaved Hossain Khan, M. A novel and highly efficient Ag and GO co-synthesized ZnO nano photocatalyst for methylene blue dye degradation under UV irradiation. *Environ. Nanotechnol., Monit. Manage.* **2021**, *16*, No. 100495.
(66) Saranya, A.; Murad, A.; Thamer, A.; Priyadharsan, A.; Maheshwaran, P. Preparation of Reduced ZnO/Ag Nanocomposites by a Green Microwave-Assisted Method and Their Applications in Photodegradation of Methylene Blue Dye, and as Antimicrobial and Anticancer Agents. *ChemistrySelect* **2021**, *6* (16), 3995−4004.
(67) Faisal, S.; Jan, H.; Shah, S. A.; Shah, S.; Khan, A.; Akbar, M. T.; Rizwan, M.; Jan, F.; Wajidullah; Akhtar, N.; Khattak, A.; Syed, S. Green Synthesis of Zinc Oxide (ZnO) Nanoparticles Using Aqueous Fruit Extracts of Myristica fragrans: Their Characterizations and Biological and Environmental Applications. *ACS Omega* **2021**, *6* (14), 9709−9722.
(68) Sivakumar, S.; Robinson, Y.; Mala, N. A. Studies on photocatalytic performance and supercapacitor applications of undoped and Cu-doped ZnO nanoparticles. *Appl. Surf. Sci. Adv.* **2022**, *12*, No. 100344.
(69) Shidpour, R.; Simchi, A.; Ghanbari, F.; Vossoughi, M. Photodegradation of organic dye by zinc oxide nanosystems with special defect structure: Effect of the morphology and annealing temperature. *Appl. Catal., A* **2014**, *472*, 198−204.
(70) Zhou, H.; Fan, T.; Zhang, D. Biotemplated materials for sustainable energy and environment: current status and challenges. *ChemSusChem* **2011**, *4* (10), 1344−1387.
(71) Saravanan, R.; Gracia, F.; Stephen, A.Basic Principles, Mechanism, and Challenges of Photocatalysis. In *Nanocomposites for Visible Light-Induced Photocatalysis*; Springer, 2017; pp 19−40 .
(72) Lakshmi, S.; Renganathan, R.; Fujita, S. Study on TiO2-mediated photocatalytic degradation of methylene blue. *J. Photochem. Photobiol., A* **1995**, *88* (2−3), 163−167.
(73) Nguyen Thi Thu, T.; Nguyen Thi, N.; Tran Quang, V.; Nguyen Hong, K.; Nguyen Minh, T.; Le Thi Hoai, N. Synthesis, characterisation, and effect of pH on degradation of dyes of copper-doped TiO2. *J. Exp. Nanosci.* **2016**, *11* (3), 226−238.
(74) Sahu, P.; Das, D. ZnO-Nanorod/Ag2O-Nanoparticle/rGO-Nanosheet Heterostructures as Photocatalysts for Enhanced Degradation of Harmful Aqueous Phase Contaminants under Extended Visible Light Exposure. *ACS Appl. Nano Mater.* **2023**, *6* (24), 22730−22744.
(75) Wang, S.; Guan, Y.; Wang, L.; Zhao, W.; He, H.; Xiao, J.; Yang, S.; Sun, C. Fabrication of a novel bifunctional material of BiOI/Ag3VO4 with high adsorption−photocatalysis for efficient treatment of dye wastewater. *Appl., Catal., B* **2015**, *168−169*, 448−457.
(76) Mohammed, A. M.; Mohtar, S. S.; Aziz, F.; Aziz, M.; Ul-Hamid, A. Cu2O/ZnO-PANI ternary nanocomposite as an efficient photocatalyst for the photodegradation of Congo Red dye. *J. Environ. Chem. Eng.* **2021**, *9* (2), No. 105065.
(77) Abel Noelson, E.; Anandkumar, M.; Marikkannan, M.; Ragavendran, V.; Thorgersen, A.; Sagadevan, S.; Annaraj, J.; Mayandi, J. Excellent photocatalytic activity of Ag2O loaded ZnO/NiO nanocomposites in sun-light and their biological applications. *Chem. Phys. Lett.* **2022**, *796*, No. 139566.
(78) Alhokbany, N.; Ahamad, T.; Alshehri, S. M. Fabrication of highly porous ZnO/Ag2O nanoparticles embedded in N-doped graphitic carbon for photocatalytic degradation of tetracycline. *J. Environ. Chem. Eng.* **2022**, *10* (3), No. 107681.
(79) Liu, S.; Jiang, X.; Waterhouse, G. I. N.; Zhang, Z.-M.; Yu, L.-m. A novel Z-scheme NH2-MIL-125(Ti)/Ti3C2 QDs/ZnIn2S4 photo-

https://doi.org/10.1021/acsomega.3c08051
ACS Omega 2024, 9, 13714−13727

catalyst with fast interfacial electron transfer properties for visible light-driven antibiotic degradation and hydrogen evolution. *Sep. Purif. Technol.* **2022**, *294*, No. 121094.
(80) Wei, Z.; Liu, J.; Shangguan, W. A review on photocatalysis in antibiotic wastewater: Pollutant degradation and hydrogen production. *Chin. J. Catal.* **2020**, *41* (10), 1440−1450.

https://doi.org/10.1021/acsomega.3c08051
ACS Omega 2024, 9, 13714−13727